Evaluation of Chitosan/Bi_2O_2S Engineered Photocatalytic Film for Visible Light Stimulated Photocatalytic Degradation of Pharmaceutical Drugs

D. Sharma[1], A. Kaur[1], S. Pathak[1], A. Dan[2]* and S. Singhal[1]*

[1] Department of Chemistry and Centre for Advanced Studies in Chemistry, Panjab University, Chandigarh 160014, India

[2] Department of Applied Chemistry, Maulana Abul Kalam Azad University of Technology, Simhat, Haringhata, West Bengal 741249, India

Email: sonal1174@gmail.com; sonal@pu.ac.in

Received: 2.1.2026, Revised: 16.1.2026, 21.1.26, Accepted: 25.1.2026

Abstract

The growing interest in environmentally benign materials has driven the development of biopolymer-based systems for wastewater remediation. In this work, chitosan-based photocatalytic hydrogel film hybridized with Bi_2O_2S sub-micron particles was designed and fabricated for the efficient removal of pharmaceutical contaminants from wastewater. A comprehensive set of analytical techniques (including; FTIR, XRD, XPS, FE-SEM, DLS, UTM, and UV-vis) were employed to confirm the successful incorporation and interaction of Bi_2O_2S sub-micron particles within the chitosan network. The mechanical integrity of the fabricated film was evaluated using a universal tensile testing machine, demonstrating enhanced mechanical strength and robustness of the nanocomposite film. The prepared photocatalytic film exhibited highly efficient visible-light-driven photocatalytic degradation of the pharmaceutical drug doxorubicin (DOX), achieving a maximum degradation efficiency of approximately 95 % within 60 min. of irradiation. Furthermore, the photocatalytic film showed an excellent structural stability which can be attributed to the strong mechanical framework and stabilizing role of the chitosan hydrogel matrix. The chitosan film acted as a multifunctional platform by providing structural support, adsorption sites for pollutant molecules, and effective immobilization of Bi_2O_2S sub-micron particles, thereby enhancing photocatalytic performance. Owing to their green synthesis route, cost-effectiveness, mechanical durability, and operational simplicity, the developed chitosan-Bi_2O_2S photocatalytic film demonstrates a strong potential for application in advanced and sustainable wastewater treatment technologies.

DOI: 10.59143/isas.jisas.4.3.FANN9260

Keywords: Chitosan, Bi_2O_2S, catalytic film, waste water treatment, Photocatalytic degradation.

1. Introduction

Rapid industrial growth and raising economic activity have intensified water pollution and health-pertinent concerns globally[1]. Numerous contaminants originating from the textile, food, paper and pharmaceutical industries, are known to be frequent toxins of wastewater[2,3]. Therefore, it is critical to use a technique that can break down toxins straight into non-toxic components like carbon dioxide and water. Several chemical, physical and biological techniques such as biodegradation[4], oxidation[5], chemical coagulation[6], adsorption[7], membrane separation[8] and photodegradation[9] have been employed to withdraw toxins from wastewater. Among these photocatalyst based on nanocomposites has drawn significant attention owing to their chemical stability, nature friendly characteristics, low cost and minimal toxicity[10-14]. Compared to bulk chemical compositions, small nanocomposites with sizes between 1 to 100 nm possess astounding surface-to-volume ratios, which lead to notable improvements in chemical and physical properties[15-18]. Consequently, metal oxide nanomaterials have received significant consideration due to their high surface area, and attractive optical, nano structural, thermodynamic and mechanical properties[19,20]. Various metal oxides such as Bi_2O_3[21], TiO_2[22], CdS[23], Cu_2O[24], Ag_3PO_4[25,26] etc. have been widely employed as a photocatalyst for pollutant removal from wastewater. Out of these, bismuth layered composites hold notable significance due to their ability to supress recombination and effectively separate photogenerated carriers[27]. Within this family, Bi_2O_2S has emerged as a highly promising visible-light photocatalyst, owing to its relatively low band gap, suitable band-edge positions, and enhanced charge transport properties. As a result, numerous studies have focused on synthesizing Bi_2O_2S nanoparticles through diverse preparation methods to evaluate and optimize their photocatalytic degradation performance [28,29].

Nevertheless, these nanoparticles have several drawbacks, such as difficult post-treatment, the possibility of secondary contamination, and nanoparticle aggregation. To overcome these limitations, various supports- including gels[30], foams[31], nanocomposites[32], and membranes[33] have been employed to immobilize the catalysts. Hydrogels, in particular, have emerged as highly effective materials for wastewater treatment due to their superior

mechanical strength, biodegradability, biocompatibility, three-dimensional network structure, insolubility in water, and high swelling capacity[34,35]. The incorporation of polymers further enhances the stability of metal oxides and promotes stronger physicochemical interactions between the catalyst and support, resulting in improved catalytic efficiency and more effective degradation[36,37].

Polyvinyl alcohol (PVA), polyvinyl chloride (PVC), polyvinyl pyrrolidone (PVP), and chitosan (CS) are examples of natural and synthetic polymers that have garnered a lot of interest for the creation of composites that are both environmentally friendly and structurally sound[38-40]. Through complexation or ion-pair formation, polymers can interact with metal ions to stabilize metal oxide nanostructures and modify their physicochemical characteristics[41]. CS is a biodegradable and biocompatible polyaminosaccharide that is rich in hydroxyl and amino groups. It has a strong ability to bind metal ions and can be used as a template to create thin photocatalytic films. These characteristics make CS-based hydrogels especially promising for use in water remediation and photocatalytic dye degradation. For example, Gupta *et al.* reported 3D engineered CS hydrogels embedded with sulfur-doped C_3N_4/ZnO nanoparticles for the photocatalytic removal of pharmaceutical pollutants[42], while Kadhim *et al.* demonstrated effective adsorption of DOX-hydrochloride onto a CS-poly (acrylic acid)/MWCNTs nanocomposite[43]; collectively, these studies highlight the potential of polymer-based matrices in designing high-performance materials for the removal of drug contaminants from water.

In response to the growing environmental threat posed by pharmaceutical contaminants, this work reports the development of an efficient photocatalytic film composed of CS coupled with Bi_2O_2S nanosheets, designed as a “dip-catalyst” for the photocatalytic degradation of DOX. Among cytostatic drugs, DOX is one of the most widely used chemotherapeutic agents for cancer treatment, and its frequent detection in wastewater raises serious environmental and public health concerns. Even at trace concentrations, DOX exhibits pronounced toxicity, with the potential to disrupt aquatic ecosystems by adversely affecting the growth, reproduction, and survival of aquatic organisms[44-45]. To the best of author’s knowledge, no prior reports have explored the photocatalytic degradation of DOX using a CS-embedded bismuth oxysulfide film. In this work, Bi_2O_2S nanosheets were incorporated into a CS hydrogel matrix via a single-pot synthesis route to produce a stable, flexible, and

mechanically robust composite film. The synthesized materials were comprehensively characterized in terms of their morphological, structural, and spectroscopic properties using various analytical techniques. Finally, the photocatalytic performance of the composite film was systematically investigated under visible-light irradiation using DOX as a model pharmaceutical pollutant, and scavenger experiments were conducted to elucidate the role of active charge carriers involved in the degradation mechanism.

2. Experimental

2.1. Materials

Bismuth (III) nitrate pentahydrate (Bi $(NO_3)_3.5H_2O$) was procured from Sisco Research Laboratories (SRL), India. The surfactant Cetyltrimethylammonium Bromide (CTAB), lithium oxide monohydrate ($LiOH.H_2O$) and thiourea were purchased from Central Drug House (P) Ltd (CDH). Isopropyl alcohol, p-benzoquinone, ammonium oxalate was obtained from TCI chemicals. Biopolymer CS was procured from SRL, India. Glutaraldehyde (GA), and sodium hydroxide (NaOH) were purchased from Merck, India and Fisher-Scientific, respectively. Industrial water was gathered from the industrial sector of Bhagwanpur in Uttarakhand, India. The target pollutant, DOX, was procured from a pharmaceutical store in Chandigarh. The distilled water used for each experiment was derived from an ultra-filtration system (Milli-Q, Millipore).

2.2. Synthesis of Bi_2O_2S and CS loaded Bi_2O_2S film

2.2.1. Preparation of Bi_2O_2S nanosheets

Bi_2O_2S was synthesized via a CTAB-assisted hydrothermal route[46]. Initially, 0.6 g of cetyltrimethylammonium bromide (CTAB) was dissolved in 80 mL of deionized water under continuous magnetic stirring for 30 min. to obtain a clear and homogeneous solution. To improve molecular dispersion, the solution was further treated ultrasonically for 20 min. Subsequently, 1.2 g of bismuth nitrate pentahydrate [Bi $(NO_3)_3 \cdot 5H_2O$] and 0.09 g of thiourea (CH_4N_2S) were added sequentially under constant stirring. The alkalinity of the reaction medium was then adjusted by the gradual addition of 3 g of lithium hydroxide monohydrate ($LiOH \cdot H_2O$), raising the pH to approximately 14. The mixture was vigorously stirred for an additional 30 min. resulting in a red-colored suspension, demonstrating the initiation of Bi-S-O formation. The resulting suspension was transferred into a 150 mL polytetrafluoroethylene (PTFE)-lined stainless steel autoclave and subjected to hydrothermal treatment at 200 ºC for 90 min. After the hydrothermal reaction, the autoclave was allowed to cool naturally to room temperature. The obtained precipitate was separated,

washed thoroughly three times with deionized water followed by an absolute ethanol to remove unreacted species and residual surfactant, and then dried overnight in a vacuum oven at 70 ºC. The final product was collected as dark red Bi_2O_2S powder.

2.2.2. Preparation of CS doped Bi_2O_2S film

The CS@Bi_2O_2S film was modelled through the ex-situ incorporation of Bi_2O_2S sub-micron particles into the CS hydrogel framework, as illustrated in (Scheme 1). Firstly, a calculated amount of CS was dissolved in 15 mL of 1% (v/v) CH_3COOH solution and stirred for 3h to produce a homogeneous solution. To this stirring solution, an aqueous dispersion of Bi_2O_2S sub-micron particles (molar ratio CS: Bi_2O_2S = 1:0.5) was added followed by the addition of cross-linker GA (60µL). The resulting solution was stirred at~40 ºC until the tight hydrogel was obtained. The hydrogel composite was casted on a petri-dish and dried at 50 ºC for 24h. The film was peeled off and subjected to a neutralizing process after drying. To neutralize the film and remove the excess acid, the composite was immersed in 0.2M NaOH for 5 min. Following neutralization, the film was cleaned once again and dried at 50 ºC. For the sake of simplicity, Bi_2O_2S is labelled as BS and CS film with embedded BS sub-micron particles as CS@BS.

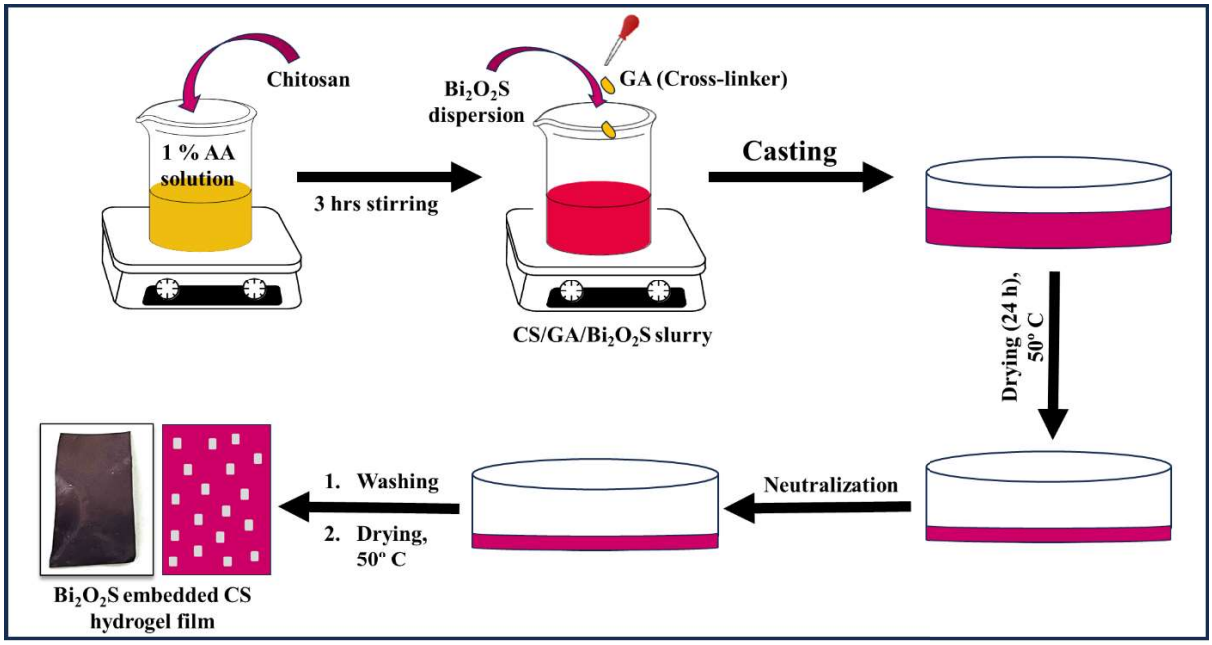

Scheme 1. Illustration of the key steps involved in the synthesis of CS@BS film.

2.3.Characterization

Several analytical methods were used to investigate the morphological characteristics and physicochemical characteristics of the prepared materials. Phase purity and structure was

examined by powder X-ray diffraction (P-XRD) in the 2θ range of 10º to 80º on Panalytical X'Pert Pro diffractometer, UK. Functional groups existing in the prepared materials were analyzed by recording Fourier transform infrared (FT-IR) spectra in the range of 4000–400 cm^{-1} on Thermo Scientific Nicolet iS50 FTIR Spectrometer. The elemental composition and chemical valencies were studied with Thermo Fisher Scientific, K- ALPHA, X-ray photoelectron spectroscopy (XPS) instrument. The deconvolution of all XPS spectra was performed using a Shirley background method to ensure accurate baseline subtraction. The FWHM for all fitted peaks was maintained within a consistent range of 1.3-1.6 eV to ensure physical reliability. Furthermore, specific fitting constraints were applied to the Bi 4f doublet, including a fixed 4:3 area ratio and a spin-orbit splitting of~ 5.3 eV, ensuring the model adheres to quantum mechanical principles. The goodness-of-fit was further validated by an Adjusted R^2 of 0.999. The morphology of synthesized material was determined by Field Emission Scanning Electron Microscopy (FE-SEM) on Hitachi-SU8010, Germany. Using a Malvern Zetasizer Nano S90 equipment with a 633 nm He-Ne laser light source, dynamic light scattering (DLS) measurements were performed at a scattering angle of 90º to determine the hydrodynamic radius and polydispersity index (PDI) of the materials. A universal tensile testing machine (UTM, BISS) was used to test the mechanical characteristics of the film. The thermal characteristics of the samples were analyzed in the temperature range of 25–1000 ºC by utilizing a SDT-Q-600 thermogravimetric analysis (TGA) instrument. A JASCO model V-750 UV–visible spectrophotometer was used for optical investigations and Photoluminescence (PL) spectra were captured using an Agilent Cary Eclipse fluorescence spectrophotometer.

2.4. Photocatalytic analysis

At room temperature, all photocatalytic tests were carried out under ideal circumstances. Using the as-synthesised film, photocatalytic degradation of a specific model pollutant was investigated using a 400 W Hg lamp running at 220 V as an artificial source of visible light illumination. In a typical experiment, the dried film (CS@BS) was added to the contaminated solution and held for 30 minutes while stirring in the dark to reach the adsorption-desorption equilibrium. A UV-visible spectrophotometer was then utilized to measure the residual concentration of contaminant after removing a fixed aliquot of 3 mL from the reaction suspension at predetermined intervals.

3. Results and Discussion

3.1. Characterization of BS and CS@BS film

3.1.1. Structural characterizations: P-XRD, FTIR and XPS

Structural characteristics, phase composition and phase purity of the prepared materials was analysed through P-XRD measurements. (Fig. 1a) depicts the P-XRD patterns recorded for BS sub-micron particles and CS@BS photocatalytic film. The diffraction peaks of BS exhibited characteristic peaks at 2θ = 14.9º (020), 24.3º (110), 30.0º (040), 32.3º (130), 45.0º (141), 45.6º (060), 47.5º (002), 57.3º (161), 59.3º (170), 62.3º (080), and 72.5º (261), which validates the formation of orthorhombic structure of BS, matching the standard data of JCPDS No. 34-1493[47]. The lattice parameters were determined to be a = 3.871 Å, b = 3.874 Å, and c = 12.131 Å. The average crystallite size (D) was determined to be 31.2 nm via the Scherrer equation, where the calculations were performed using the most intense (130) peak. This size confirms the nanocrystalline nature of the BS particles. In contrast, the diffraction peaks of CS@BS reveals that the presence of polymer film sacrifices the crystallinity of the embedded particles and reduced the inclusive long-range ordering of the sub-micron particles. Interestingly, while most peaks exhibit a downward trend, the (040) diffraction peak at 30.0º maintains a notable degree of stability and shows a marginal relative enhancement compared to other crystallographic planes. This phenomenon suggests that the (040) plane serves as a primary interfacial site for interaction or preferential alignment within the polymer framework. Overall, the integration of BS sub-micron particles into the CS hydrogel resulted in a perceptible reduction in the intensity of the diffraction peaks in the XRD pattern of the composite material due to CS induced amorphous character.

FTIR spectroscopy was performed to confirm the successful incorporation of BS sub-micron particles into the CS hydrogel matrix and to investigate the molecular interactions within the composite (Fig. 1b). The FTIR spectrum of pristine BS exhibited characteristic bands between 450 and 500 cm^{-1}, corresponding to Bi-S vibrations, while the peak at 517 cm^{-1} was assigned to Bi-O stretching. A band at 845 cm^{-1} was attributed to carbonate (CO_3^{2-}) species[48], and the absorption at 1025 cm^{-1} arose from C-O stretching vibrations[49]. Weak peaks at 2850 and 2916 cm^{-1}, along with bands in the 1415-1539 cm^{-1} region, were associated with C-H stretching of $-CH_3$ and $-CH_2$ groups, indicating trace ethanol adsorption during washing. Additionally, a broad band at 3487 cm^{-1} corresponded to O-H stretching of adsorbed water molecules[50]. In the CS@BS composite film, notable changes in the FTIR

spectrum indicated interactions between BS sub-micron particles and the CS matrix. The Bi-O band shifted and weakened to ~511 cm^{-1}, suggesting strong interfacial interaction. The broad band around 1010 cm^{-1} was attributed to C-O-C stretching of the CS backbone, while broadening near 1347 cm^{-1} indicated modifications of -CH_2 vibrations. Peaks at 1553 cm^{-1} and 1634 cm^{-1} corresponded to N-H bending of CS amino groups and amide vibrations, respectively. The bands at 3270 cm^{-1} and 1739 cm^{-1} were assigned to O-H stretching and C=O stretching, respectively. Furthermore, reduced intensity of the band near 2867 cm^{-1} reflected weakening of -CH_3 vibrations from residual ethanol[51,52]. Overall, the observed peak shifts and intensity changes confirm the successful incorporation of BS sub-micron particles into the CS hydrogel and suggested strong interfacial interactions between the polymer matrix and the sub-micron particles, which likely contributed to the enhanced structural stability and functionality of the composite film.

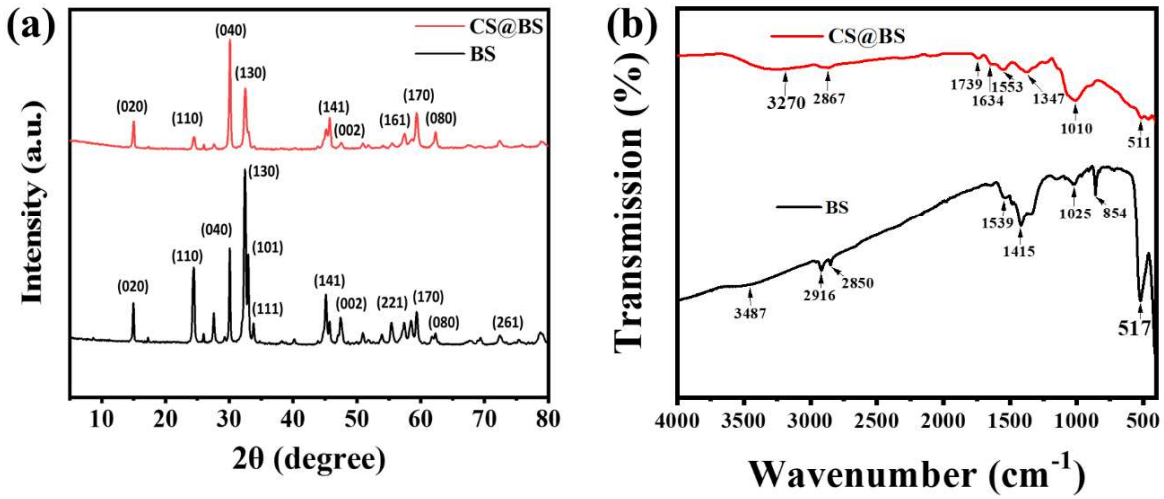

Fig. 1. (a) Powder XRD patterns and (b) FT-IR spectra of the as-synthesized BS sub-micron material and CS@BS film. [BS: Bi_2O_2S; CS@BS: Chitosan loaded with BS]

X-ray photoelectron spectroscopy (XPS) was employed to examine the surface chemical composition and electronic states of the CS@BS composite film, as shown in Fig. 2. The survey spectrum (Fig. 2a) confirms the presence of the major constituent elements C, N, O, Bi, and S, with characteristic binding energies observed at 286.0 eV (C 1s), 398.1 eV (N 1s), 531.6 eV (O 1s), 157.3 eV (Bi 4f), and 162.5 eV (S 2p), respectively, indicating the successful formation of the CS@BS film. The high-resolution C 1s spectrum (Fig. 2b) can be deconvoluted into three distinct components centred at 284.6 eV, 286.3 eV, and 288.1 eV, which are attributed to C–C/C–H, C–O/C–N, and O–C–O (acetal or carbonyl-related) functional groups, respectively, originating from the CS backbone[53]. The N 1s spectrum

(Fig. 2c) exhibits two characteristic peaks at 398.1 eV and 401.5 eV, corresponding to -NH- and protonated amine ($–NH_X$) species, respectively, confirming the presence of amine functionalities inherent to the CS matrix. The O 1s spectrum (Fig. 2d) shows two peaks centred at 530 eV and 531.6 eV, which were primarily associated with Bi-O and C=O bonds, suggesting the coexistence of oxygen-containing functional groups from CS and oxygen coordination in the bismuth oxy-sulphide framework. The high-resolution Bi 4f spectrum (Fig. 2e) displays two well-defined peaks at 157.3 eV (Bi $4f_{7/2}$) and 162.5 eV (Bi $4f_{5/2}$), characteristic of Bi^{3+} species. These peaks are attributed to Bi-O and Bi-S bonding environments, confirming the incorporation of bismuth oxy-sulphide within the composite structure[54]. Furthermore, the S 2p spectrum (Fig. 2f) exhibits a prominent peak at ~162 eV, which is assigned to sulphide sulphur (S^{2-}), providing strong evidence for the presence of Bi-S bonds in the CS@BS composite. Overall, the simultaneous detection of C, N, and O from CS together with Bi and S from the bismuth oxy-sulphide phase confirms the effective embedding of BS within the CS matrix.

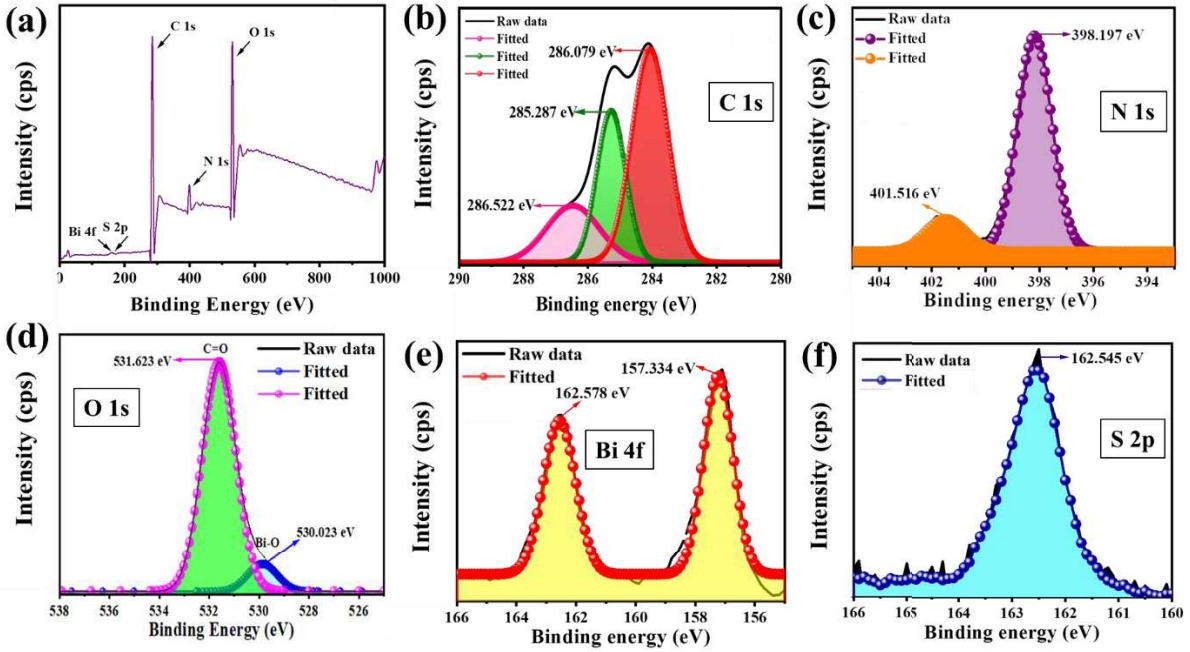

Fig. 2. (a) XPS survey and high resolution deconvoluted XPS spectra of (b) C 1s, (c) N1s, (d) O 1s, (e) Bi 4f, and (f) S 2p scan for CS@BS film.

3.1.2. Morphological characterization

The morphological characteristics of the fabricated CS@BS film were examined using Field Emission Scanning Electron Microscopy (FE-SEM) (Fig. 3). The low-magnification image (Fig. 3a) reveals a uniform and continuous distribution of BS particles over the surface of hydrogel matrix, while the high-magnification images (Fig. 3(b-c)) clearly demonstrate the

characteristic brick-like morphology of BS nanosheets embedded in the hydrogel film. The preservation of this distinct morphology indicates that the CS hydrogel network does not alter or disrupt the inherent structural features of BS sub-micron particles during film formation.

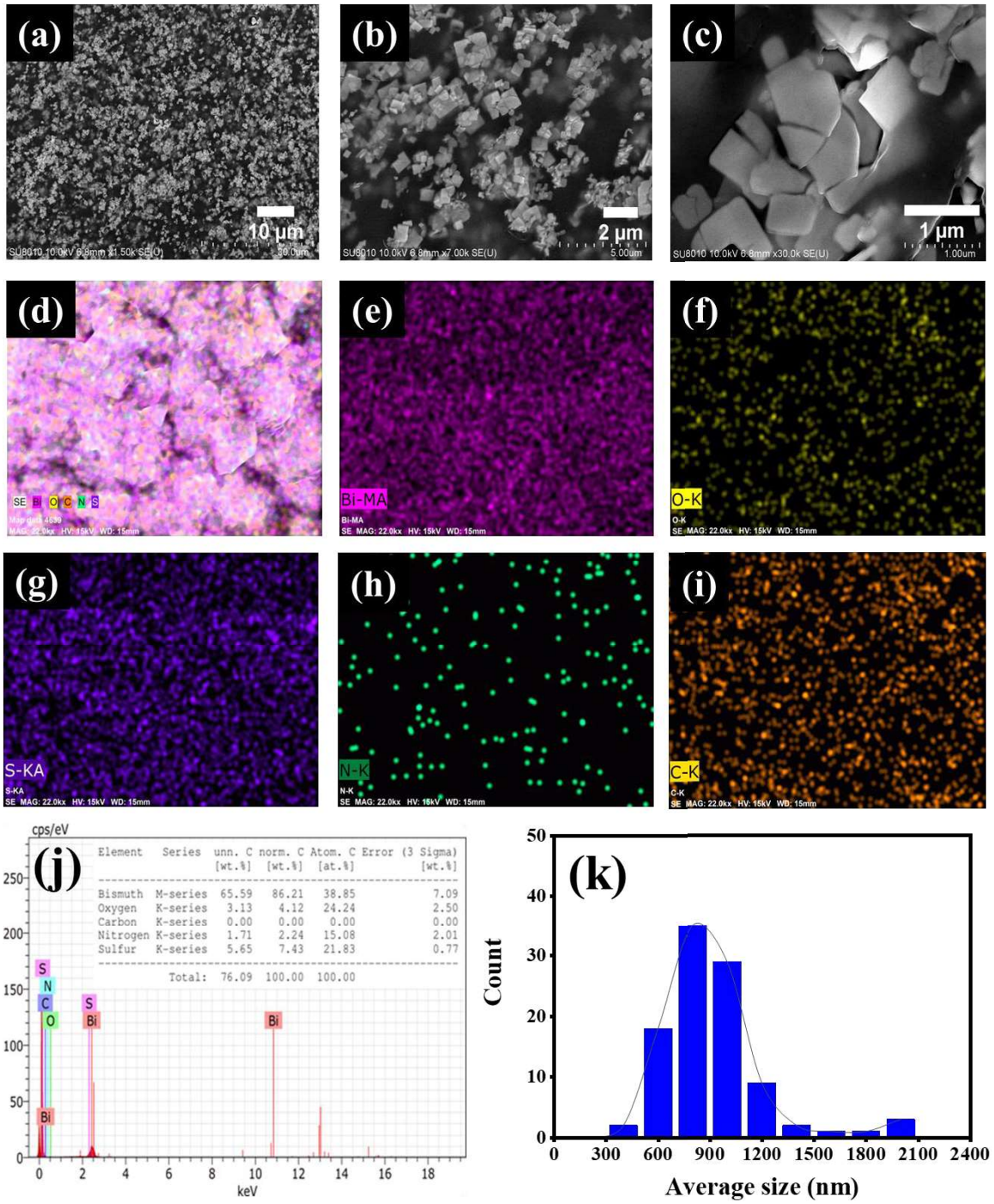

Fig. 3. (a) Low magnification and (b-c) High magnification FE-SEM micrographs of CS@BS film; elemental mapping of (d) CS@BS film, (e) Bi distribution, (f) O distribution, (g) S distribution, (h) N distribution, (i) C distribution, (j) EDS spectra, and (k) size distribution of BS sub-micron particles embedded in CS film.

Furthermore, the elemental composition of the film was confirmed by Energy-Dispersive X-ray Spectroscopy (EDS) analysis (Fig. 3(d-h)), which quantifies the presence of the major constituent elements, namely Bi, S, O, and N, confirming the successful incorporation of BS sub-micron particles into the CS film (Fig. 3j). The EDS quantitative investigation confirms the production of BS, with Bi and S concentrations of 38.85 and 21.83 at%, respectively. The elemental mapping reveals a consistent distribution of Bi and S across the sample, indicating high compositional homogeneity. However, quantitative estimation of carbon could not be obtained from the EDS analysis. This limitation arises from the inherent constraints of conventional EDS in accurately detecting and quantifying low-atomic-number elements, particularly in polymeric materials. In polymers such as CS, the low-energy X-ray signals generated by carbon are weak and prone to absorption and background interference, leading to unreliable quantitative results. Consequently, carbon is often excluded from EDS compositional analysis, despite its clear presence in elemental mapping[55]. The (Fig. 3k) depicts the particle size distribution of the embedded BS sub-micron particles, revealing an average particle size of 900 ± 200 nm. Additionally, the hydrodynamic radius (R_h) of bare BS sub-micron particles was analysed using DLS (Fig. 4a). For measurement 5×10^{-4} g/mL of BS sub-micron particle dispersion was utilized by equilibrating the sample for 60 sec before each measurement. The DLS shows the average size of BS sub-micron particles around 984.5 ± 73.2 nm (PDI= 0.2 ± 0.1), corroborating the FESEM findings.

3.1.3. Mechanical strength

The mechanical strength of the CS@BS and CS film was analysed using universal testing machine (UTM) (Fig. 4b)**.** The CS@BS photocatalytic film and CS film were cut into a block (16.61 mm in length, 9.53 mm in width and 0.09 thickness) and stretched with an extension rate of 10 mm/min[56]. The Pure CS film showed more ductile behaviour, with higher elongation but lower peak load (axial load 6.6 N) (Fig. 4b). In contrast, the CS@BS film had a substantially steeper initial slope and a greater tensile strength of 9.16 MPa (axial load 7.8 N). While the addition of BS resulted in a 6.9 % decrease in elongation, the increased peak load demonstrates that the inorganic filler serves as a reinforcement agent. This improvement in stiffness and strength is critical for the film's stability as a dip-catalyst, preventing structural deformation or ripping when used repeatedly in aquatic conditions.

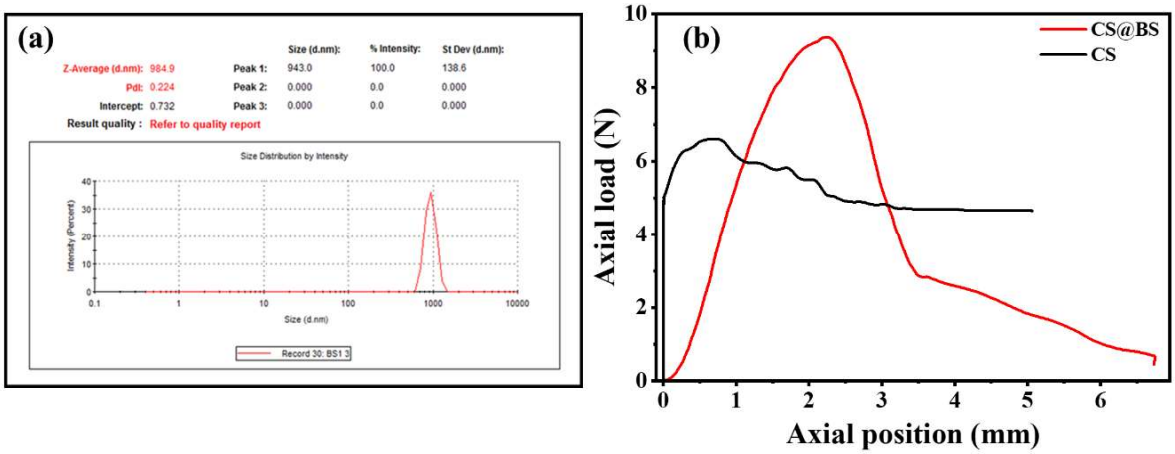

Fig. 4. (a) DLS spectra of BS sub-micron particles and (b) mechanical strength of CS@BS and CS film with an axial load and position curve.

3.1.4. Thermal and optical measurements: TGA/DSC and UV-vis DRS

The Thermogravimetric analysis (TGA) technique was employed to examine the thermal behaviour of the synthesized materials (Fig. 5a). The BS sub-micron particles depicted higher thermal stability with negligible weight loss up to 800 ºC. This minimal decomposition could be attributed due to loss of adsorbed moisture adsorbed and weakly bonded volatile species existing on the surface of sub-micron particles. The corresponding DSC thermogram of BS indicates the prominent endothermic peak around 310 ºC which indicates the formation of $Bi_4O_4S_3$ by heating of BS sub-micron particles (Fig. 5a). On heating, BS undergoes a decomposition-driven phase transformation. BS consists of alternating layers of $[Bi_2O_2]^{2+}$ separated by S^{2-} anions. The structure was loosely packed, making it susceptible to thermal decomposition. $Bi_4O_4S_3$ also contains $[Bi_2O_2]$ layers, but additionally includes Bi-S layers and sulfur vacancies. This structural similarity allowed a topotactic-like transformation rather than complete breakdown[57]. In contrast, the CS@BS film displayed a different weight loss pattern with rise in temperature. The hydrogel film lost ~40% of its weight over two consecutive thermal events. In first decomposition step (~ below 250 ºC), the initial decomposition could be accredited to the weight loss due to adsorbed water molecule and volatile species. The structural stability and functionality of hydrogel systems depend heavily on the adsorption of a significant number of water molecules. In second step (~ above 250 ºC), the substantial change in thermogram slope shows slower rate of degradation which suggests the release of CH_4 from the photocatalytic film[58]. the incorporation of sub-micron particles significantly restricted the weight loss to ~40%, demonstrating enhanced thermal stability due to sub-micron particle–polymer interactions. The homogenous existence of BS nanosheets overall improved the thermal

stability of the CS hydrogel network, thereby restricting the diffusion of volatile and oxygen-containing decomposition product from diffusing through the composite film[59].The corresponding DSC thermogram of CS@BS depicts a prominent endothermic peak around 310 ºC which suggested the decomposition of 2-amino-2-deoxy-d-glucopyranose (GlcN) amine group (Fig. 5a)[60].

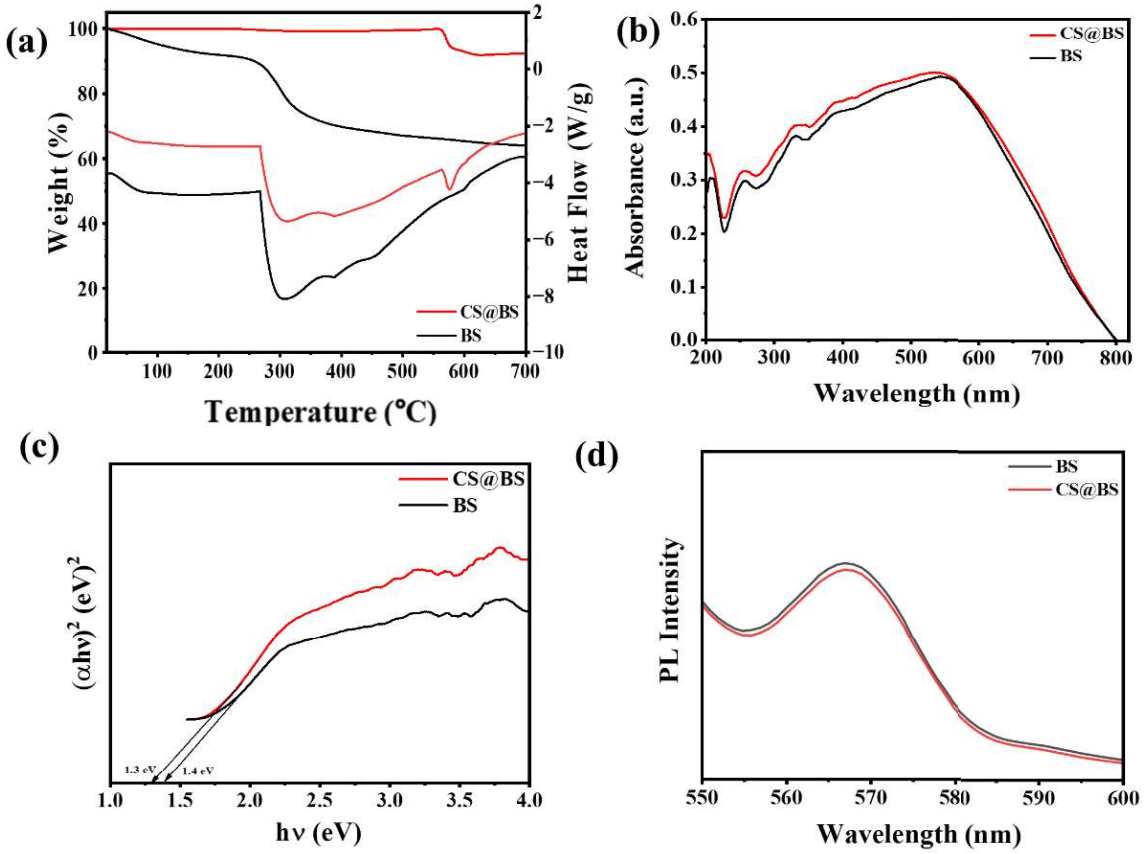

Fig. 5. (a) TGA/DSC profiles, (b) UV-vis DRS spectra, (c) Tauc plot and (d) PL spectra of the BS and CS@BS film.

The optical absorption characteristics of the synthesized materials were examined using UV-vis DRS (Fig. 5b). The spectra of the BS and CS@BS material demonstrated a broad absorption ranging from 200 to 550 nm. The electronic transitions of CS functional groups are responsible for the absorption in the deep UV region (<300 nm). BS, a narrow band gap semiconductor with intrinsic visible-light responsiveness, is responsible for the significant absorption in the UV and visible ranges. The layered structure of BS could be linked to extended absorption in the visible region. Moreover, improved dispersion and interfacial interactions, which are advantageous for photocatalytic applications, boost light harvesting when BS is included into the CS matrix. Overall, this modification increases the ability of

CS@BS film to capture visible light effectively. Additionally, the optical band gaps of the synthesized materials were evaluated to gain the deeper insights using Tauc's Eq. (1)[61]:

$$\alpha hv = A(hv - E_g)^{\frac{1}{2}} \quad (1)$$

where, α represents the absorption coefficient, h represents the Planck's constant, v represents the frequency of light, E_g represent the band gap and A represents the proportionality constant. The Tauc plot were recorded by plotting curves between $(\alpha hv)^2$ and hv. The band gap values were analysed by extrapolating the tangent on the curve at x-axis. The calculated band gap for BS and CS@BS film was 1.40 and 1.30 eV, respectively (Fig. 5c). This slight reduction in the band gap value after incorporation regulates the improved generation of electron-hole pairs. This decrease indicates that CS creates interfacial contacts that may promote charge transfer and enhance light usage rather than substantially changing the underlying electronic structure of BS. Furthermore, photoinduced charge carrier separation efficiency was confirmed using PL spectra. In general, high-intensity PL spectra imply a faster recombination of charge carriers, whereas low-intensity spectra indicate a slower recombination rate. As demonstrated in (Fig. 5d), the PL spectra suggest that CS@BS has lower intensity than pure BS. This predicts a lower recombination rate and better separation of photoinduced charge carriers, both of which are highly advantageous for increasing the material's photocatalytic activity.

3.2.Evaluation of photocatalytic performance

3.2.1. Control experiment

Prior to evaluating the photocatalytic activity of the synthesized materials, a series of control experiments were conducted. The aim of this investigation was to examine the effect of each factor on the degradation efficiency. The time vs. percentage degradation curve for DOX elimination under three conditions: (a) light source only, (b) catalyst only, and (c) both light source and catalyst was recorded (Fig. 6a). Typically, for a photodegradation experiment, aqueous solution of DOX (0.05 mM) was prepared. The degradation efficiencies were found to be 10 % in the presence of the light source. Additionally, thorough adsorption studies were performed for which the CS@BS film was kept in the DOX solution under dark conditions for 60 minutes. The results indicate an approximately 24 % of removal of DOX via adsorption (Fig. 6b). On the other hand, a prominent enhancement in degradation, achieving 95 % when catalyst and light source were present simultaneously. To conclude, the experiment highlights the importance of combining catalyst with light source to attain maximum removal of DOX from aqueous solution.

3.2.2. Effect of parameters

Multiple reaction parameters strongly affect photocatalytic performance, making their systematic evaluation and optimization crucial for enhancing pollutant degradation. Consequently, optimization experiments were conducted using CS@BS film as the model photocatalyst. To note, the dosage of the film was adjusted by cutting it to the right weight.

3.2.3. Effect of pH

The initial pH of the pollutant solution has a significant impact on photocatalytic performance because it influences the generation of reactive species as well as surface charge characteristics (Fig. 6c). Moreover, the CS hydrogel individually entails stimuli-responsiveness and hence the varying pH conditions can influence the efficiency of the catalyst. Thus, to assess the influence of solution pH, photocatalytic degradation tests were conducted utilizing photocatalytic film (1g/L) in various pH including 3 (acidic),7 (neutral), and 9 (basic). Under acidic conditions (pH-3), CS's excessive protonation and DOX's cationic nature cause electrostatic repulsion which decreases the extend of degradation to approximately 50 %. Nevertheless, upon increasing the pH value from 3 to 7, the degradation efficiency of the catalyst improved drastically resulting in 95 % degradation. At neutral pH, the CS surface is partially deprotonated resulting in minimal repulsion and aiding optimal adsorption of the DOX through van der Waals interactions and hydrogen bonding. This also provisions the balanced generation of $^{\bullet}OH$ and $^{\bullet}O_2^-$ radicals and also reduces the electron-hole recombination, manifesting the enhanced degradation efficiency. Under alkaline circumstances, the catalyst exhibited reduced degradation of exposed pollutant (~ 44%) and this behaviour originates from the destabilization of DOX and CS. Collectively, these observations underscore the decisive influence of pH on photocatalytic degradation, with neutral conditions (pH = 7) providing the most effective degradation performance.

3.2.4. Effect of catalyst dosage

The weight of the CS@BS film was varied from 0.5 to 1.5 g/L while maintaining a pH of 7 in order to investigate the impact of catalytic sites on the photodegradation reaction. (Fig. 6d) demonstrates that as the catalyst dose increased from 0.5 to 1 g/L, the photocatalytic performance of photocatalytic film increases from 76 to 95 %. This might be explained by increased number of catalytic reactive sites accessible for the adsorption of pollutant molecules. Nevertheless, the catalytic activity decreased (~ 73%) when the catalyst dosage was increased to 1.5 g/L because the light per unit area decreased and the film's bending

shadowed the pollutant, making visible light less accessible. As a result, the catalyst dosage for the ensuing photocatalytic reactions was 1 g/L.

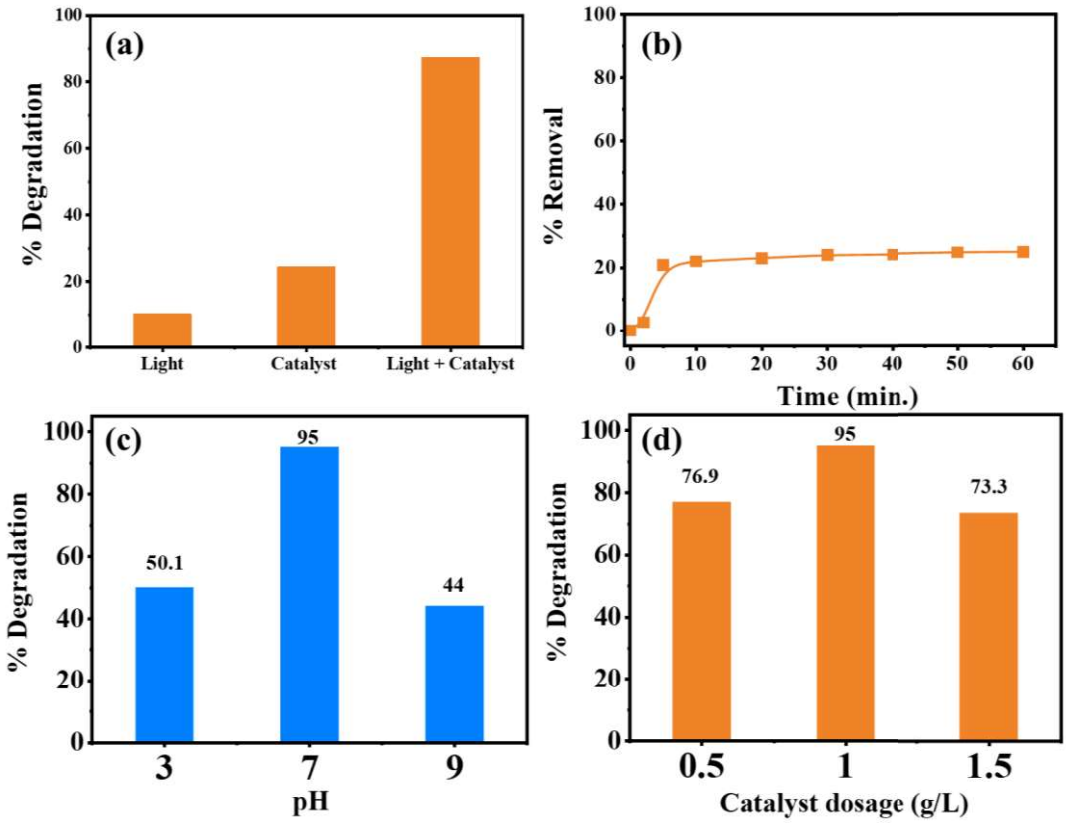

Fig. 6. (a) Comparative degradation efficiency of the pollutants under different control conditions: light only, catalyst only and light + catalyst, (b) Adsorption kinetics, (c) Effect of pH, and (d) catalyst dosage on the % degradation of DOX by CS@BS film.

3.2.5. Comparison analysis of prepared materials.

The photocatalytic activity of the BS nanocomposite and CS@BS photocatalytic film was examined through a degradation experiment, where the depletion of DOX was facilitated under visible light irradiation of 60 minutes. The percentage of pollutant degradation (%) was estimated using Eq. (2)[62]:

$$\%\ Degradation = \frac{C_o - C_t}{C_o} \times 100 \quad (2)$$

where, the absorbance of a pollutant solution at initial time (t = 0 min.) and at time t min. are represented by C_o and C_t, respectively. (Fig. 7a) depicts the % degradation vs time plot for the DOX on exposure of BS sub-micron particles and CS@BS photocatalytic film. Only the photocatalytic process was taken into consideration and further investigated because both the formed nanocomposites displayed very little adsorption under dark conditions. In the photocatalytic experiment, BS sub-micron particles displayed lower degradation efficiency

with 83% degradation of DOX in 60 min. of light irradiation. Whereas, CS@BS photocatalytic film exhibited high degradation efficacy as compared to BS with 95 % removal of DOX under similar conditions. This increased pollutant degradation can be validated using UV-DRS and PL spectroscopy analysis. The reduced band gap of CS@BS compared to pristine BS facilitated improved degradation, as demonstrated by the Tauc plot. Overall, the higher degradation efficiency could be attributed to improved DOX adsorption on CS, better dispersion of BS, and lower charge recombination due to interfacial contacts. Furthermore, the rate kinetics of DOX degradation were investigated and revealed to follow a pseudo-first-order kinetic model, as given by the Eq. (3)[60]:

$$\ln\left(\frac{C_t}{C_o}\right) = -kt \quad (3)$$

where, k is the rate constant. The rate constants were calculated using linear plots of ln (C_t/C_o) over time t, as seen in (Fig. 7b). The derived rate constants were 0.03 and 0.05 min^{-1} for BS and CS@BS, respectively. The kinetic analysis reveals that higher degradation efficiencies are accompanied by larger rate constants, with the CS@BS film achieving the maximum value, indicative of its superior photocatalytic performance. This makes CS@BS a highly effective catalyst for the breakdown of harmful contaminants in water systems, emphasizing its potential for use in environmental applications.

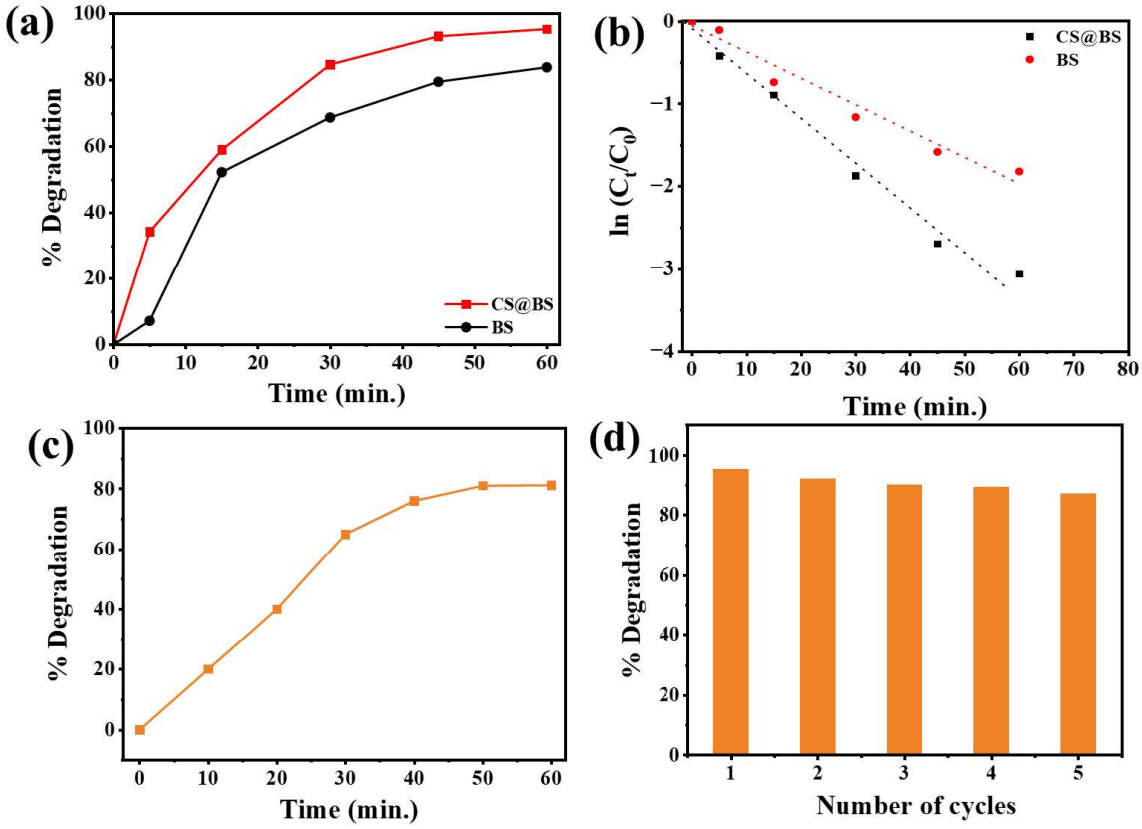

Fig. 7. (a) Photocatalytic degradation curve, (b) corresponding reaction kinetic plots of CS@BS film, (c) photocatalytic degradation of real pharmaceutical wastewater, and (d) recyclability studies of CS@BS film upto five consecutive cycles.

3.2.6. Real sample analysis, recyclability, reusability and stability studies.

After evaluating the synthesized catalyst in a distilled water matrix, its practical applicability was further examined using real wastewater collected from Bhagwanpur, Uttarakhand (India), which was spiked with DOX (25 mg L^{-1}). Under visible-light irradiation at neutral pH, the CS@BS film achieved approximately **81% degradation within 60 min,** demonstrating effective photocatalytic activity even in complex wastewater matrices (Fig. 7c). These results indicate that the presence of background impurities in industrial water does not significantly hinder the performance of the photocatalytic film. Furthermore, recyclability and reusability are critical parameters for photocatalysts intended for industrial wastewater treatment. Accordingly, the reusability of the CS@BS film was evaluated over **five consecutive cycles**. After each cycle, the film was recovered using forceps, thoroughly rinsed with distilled water, and dried at 50 ºC prior to reuse. The photocatalyst retained a degradation efficiency of approximately **86% after five cycles** (Fig. 7d), indicating good operational stability. Additionally, FTIR analysis was employed to assess possible structural or compositional changes in the regenerated catalyst. The

characteristic absorption bands of CS, including the N-H bending vibration at ~1553 cm^{-1} and the O-H stretching vibration at ~3270 cm^{-1}, along with the vibrational features associated with the BS framework, remained unchanged in both position and intensity after repeated use (Fig. 8a). The preservation of these spectral features confirms the excellent photostability of the composite film and its resistance to photocorrosion or chemical degradation during DOX treatment.

3.2.7. Scavenger studies.

Scavenger experiments were executed to explore the roles of the main reactive species engaged in photocatalytic degradation (Fig. 8b). The studies were performed at fix reaction conditions involving, [catalyst] = 1g /L, pH = 7, [DOX] = 0.05mM, and light irradiation time = 60 min. Isopropyl alcohol (IPA), ammonium oxalate (AO), and p-benzoquinone (p-BQ) were taken as scavengers for $^{\bullet}OH$, h^{+}, and $^{\bullet}O_2^{-}$, respectively. On exposure of p-BQ and AO, a considerable decline in the degradation was recorded, with degradation efficiency of 68 % and 59 %, respectively. These outcomes significantly indicate the foremost role of $^{\bullet}O_2^{-}$ and h^{+} radicals in the photocatalytic removal of DOX using the synthesized catalyst. In contrast, upon exposure of IPA a huge decrease in the degradation efficiency was observed with a percent degradation of only 14 % in 60 min. This sharp decline in the degradation highlights the leading role of $^{\bullet}OH$ radicals in driving the removal of DOX. The contributions of the reactive species to DOX degradation follow the order $^{\bullet}OH > h^{+} > {}^{\bullet}O_2^{-}$, demonstrating that hydroxyl radicals play the dominant role in the photocatalytic removal of DOX, while photoinduced holes and superoxide radicals have comparatively less involvement. To conclude, the study highlights the importance of reactive species in accelerating the effective degradation of DOX from polluted water using CS@BS photocatalytic film.

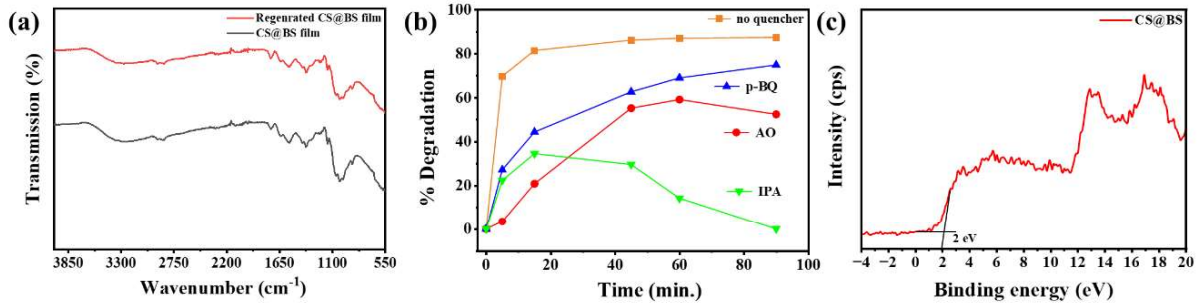

Fig. 8. (a) FTIR spectra of fresh and regenerated CS@BS film, (b) Photocatalytic degradation in the presence and absence of radical scavengers, and (c) XPS valence band spectra of CS@BS film.

3.2.8. Mechanism

The electronic band structures of pure BS and the CS@BS composite were meticulously examined in order to obtain mechanistic understanding of the photocatalytic removal of DOX in wastewater and the corresponding charge-transfer mechanisms. The band gap energy of pristine BS was found to be approximately 1.4 eV, while that of CS@BS was reduced to about 1.3 eV, indicating an enhanced light-harvesting capability after composite formation. The superior photocatalytic performance of CS@BS toward DOX degradation is attributed to its strong UV-light absorption and efficient photoinduced charge separation. The reduced band gap of CS@BS facilitates electron excitation from the valence band (VB) to the conduction band (CB), accompanied by the simultaneous generation of photogenerated holes in the VB. This efficient charge-carrier separation is crucial for driving the photocatalytic degradation process.

To further elucidate the redox ability of the photocatalyst, the valence band edge potential (E_{VB}) was experimentally determined using valence-band X-ray photoelectron spectroscopy (VB-XPS), while the conduction band edge potential (E_{CB}) was estimated using the following relationship[63]:

$$E_{CB} = E_{VB} - E_g \quad (4)$$

where, E_g is the band gap of the material obtained from DRS, E_{CB} and E_{VB} is the conduction and valence edge potential, respectively. By combining the band gap energy obtained from the Tauc plot with the E_{VB} value derived from the VB-XPS spectra (Fig. 8c), the E_{VB} of CS@BS was determined to be 2.00 eV and the corresponding E_{CB} was calculated to be approximately 0.7 eV. Based on these band positions, a plausible photocatalytic mechanism involving efficient charge transfer and reactive oxygen species (ROS) generation is proposed (Fig. 9).

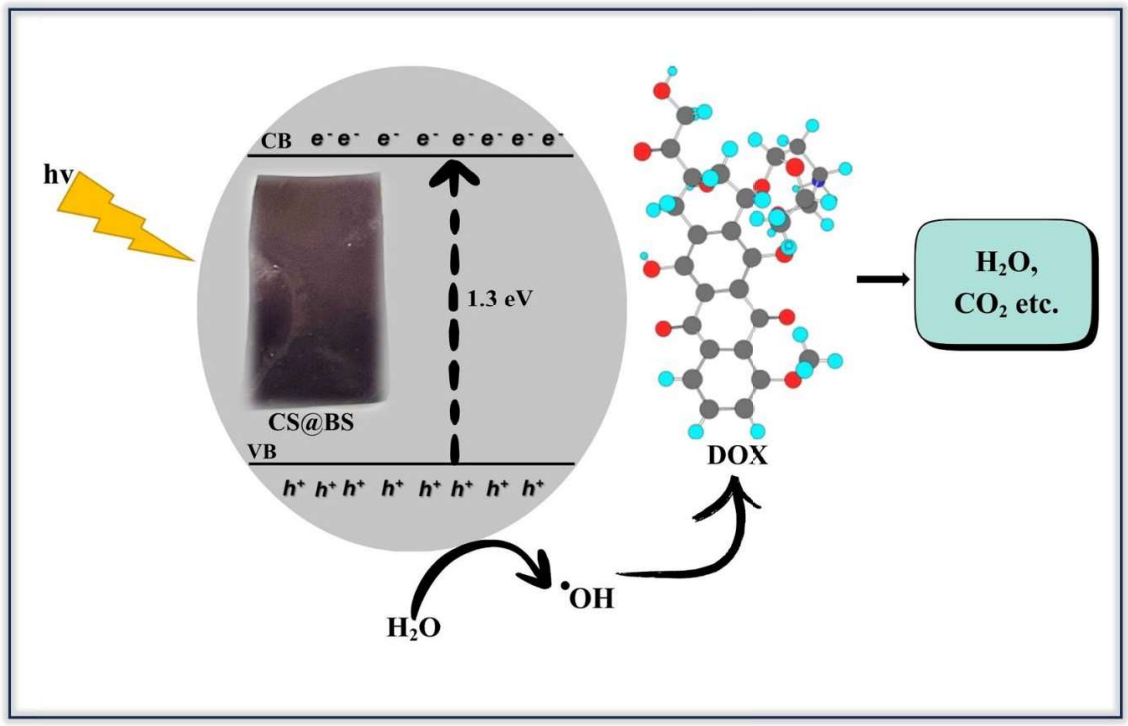

Fig. 9. The schematic representation of direct charge transfer mechanism occurring in CS@BS film.

Under UV-light irradiation, CS@BS undergoes photoexcitation as described in Eq. (5):

$$hv + CS@BS \rightarrow e^{-}(CB) + h^{+}(VB) \quad (5)$$

The photogenerated charge carriers participate in a sequence of redox reactions. The sufficiently positive valence band potential (2.00 eV), which exceeds the standard redox potential of $H_2O/^{\bullet}OH$ (1.23 eV vs. NHE)[64], enables the oxidation of water or surface hydroxyl groups to produce hydroxyl radicals ($^{\bullet}OH$), as shown in Eq. (6) and (7):

$$h^{+}(VB) + H_2O \rightarrow OH^{\bullet} + H^{+} \quad (6)$$

$$h^{+}(VB) + OH^{-} \rightarrow OH^{\bullet} \quad (7)$$

The scavenger studies imply that these highly reactive species aid in the breakdown of the DOX molecular structure into smaller, less harmful intermediates, a process that normally leads to break down into CO_2 and H_2O (or N-based byproducts) after prolonged treatment, and represented in Eq. (8):

$$DOX + OH^{\bullet} \rightarrow Degraded\ products \quad (8)$$

Overall, the enhanced photocatalytic activity of CS@BS can be attributed to its reduced band gap, favourable band-edge alignment and efficient separation of photogenerated electron–hole pairs. These features effectively suppress charge recombination and promote

ROS generation, thereby significantly improving the photocatalytic degradation efficiency of DOX under UV irradiation.

3.3.Conclusion

In summary, a smart photocatalytic film based on CS hybridized with BS (CS@BS) was successfully developed, exhibiting excellent water stability and high photocatalytic efficiency toward the degradation of DOX. The CS@BS film demonstrated approximately 95 % degradation of DOX within 60 min. of irradiation. Reactive species trapping experiments revealed that $^{\bullet}OH$ radicals were the dominant reactive oxygen species responsible for the photocatalytic degradation process. The structural analysis confirmed that BS retained its orthorhombic crystal structure even after incorporation into the CS matrix. Unlike conventional sub-micron particle-based photocatalysts, the CS-based film provides improved handling, structural integrity, and effectively suppresses catalyst leaching during operation. Furthermore, the photocatalytic film operates as a “dip-catalyst,” enabling a reversible on-off photocatalytic response that can be readily controlled by simple immersion or removal from the reaction medium. Owing to its environmentally benign composition, cost-effectiveness, operational simplicity, and high photocatalytic efficiency, the CS@BS film shows strong potential for applications extending beyond wastewater treatment.

Acknowledgement

D.S. is thankful for the support provided by the DST-Inspire fellowship for carrying out this research. The authors would like to thankfully acknowledge the RUSA 2.0, Panjab university, and Sophisticated Analytical Instrumentation Facility (SAIF-CIL), Panjab university, Chandigarh, for the required instrumental facilities.

Conflict of Interest

The authors declare no conflict of interest.

References

1. M. Aqeel, M. Ikram, A. Asghar, A. Haider, A. Ul-Hamid, M. Naz, S. Ali, 'Synthesis of capped Cr-doped ZnS nanoparticles with improved bactericidal and catalytic properties to treat polluted water', Appl. Nanoscience, 10, 2045–2055, 2020.
2. Y. Zhou, S. Fang, M. Zhou, G. Wang, S. Xue, Z. Li, C. Yao, 'Fabrication of novel $ZnFe_2O_4$/BiOI nanocomposites and its efficient photocatalytic activity under visible-light irradiation', J. Alloys Compd., 696, 353–361, 2017.

3. A. M. Elgarahy, K. Z. Elwakeel, S. H. Mohammad, G. A. Elshoubaky, 'A critical review of biosorption of dyes, heavy metals and metalloids from wastewater as an efficient and green process', Cleaner Eng. Technol., 4, 100209, 2021.
4. A. Ahmad, S. H. Mohd-Setapar, C. S. Chuong, A. Khatoon, W. A. Wani, R. Kumar, M. Rafatullah, 'Recent advances in new generation dye removal technologies: novel search for approaches to reprocess wastewater', RSC Adv., 5, 30801–30818, 2015.
5. X. Liu, Z. Chen, W. Du, P. Liu, L. Zhang, F. Shi, 'Treatment of wastewater containing methyl orange dye by fluidized three-dimensional electrochemical oxidation process integrated with chemical oxidation and adsorption', J. Environ. Manage., 311, 114775, 2022.
6. S. O. Akinnawo, P. O. Ayadi, M. T. Oluwalope, 'Chemical coagulation and biological techniques for wastewater treatment', Ovidius Univ. Ann. Chem., 34, 14–21, 2023.
7. L. L. Zhang, L. Zhan, Y. D. Jin, Z. L. Min, C. Wei, Q. Wang, Q. Yuan, 'SIRT2 mediated antitumor effects of shikonin on metastatic colorectal cancer', Eur. J. Pharmacol., 797, 1–8, 2017.
8. X. Chen, Z. Wang, S. Bi, K. Li, R. Du, C. Wu, L. Chen, 'Combining catalysis and separation on a PVDF/Ag composite membrane allows timely separation of products during reaction process', Chem. Eng. J., 295, 518–529, 2016.
9. M. S. Vasheghani Farahani, M. Nikzad, M. Ghorbani, 'Fabrication of Fe-doped ZnO/nanocellulose nanocomposite as an efficient photocatalyst for degradation of methylene blue under visible light', Cellulose, 29, 7277–7299, 2022.
10. J. B. Joo, M. Dahl, N. Li, F. Zaera, Y. Yin, 'Tailored synthesis of mesoporous TiO_2 hollow nanostructures for catalytic applications', Energy Environ. Sci., 6, 2082–2092, 2013.
11. H. Tan, Z. Zhao, M. Niu, C. Mao, D. Cao, D. Cheng, Z. Sun, 'A facile and versatile method for preparation of colored TiO2 with enhanced solar-driven photocatalytic activity', Nanoscale, 6, 10216–10223, 2014.
12. M. Ali, S. Sharif, S. Anjum, M. Imran, M. Ikram, M. Naz, S. Ali, 'Preparation of Co and Ni doped ZnO nanoparticles served as encouraging nano-catalytic application', Mater. Res. Express, 6, 1250d5, 2020.

13. D. Rosa, S. Lattanzio, I. Bavasso, L. Di Palma, 'Investigation of the synergistic effect of hydrogen peroxide and ultrasound on the photocatalytic treatment under visible light of dyes wastewater', Chem. Eng. Sci., 282, 119290, 2023.
14. M. K. Indana, B. R. Gangapuram, R. Dadigala, R. Bandi, V. Guttena, 'A novel green synthesis and characterization of silver nanoparticles using gum tragacanth and evaluation of their potential catalytic reduction activities with methylene blue and Congo red dyes', J. Anal. Sci. Technol., 7, Article no. 19, 2016.
15. T. Y. Shin, S. H. Yoo, S. Park, 'Gold nanotubes with a nanoporous wall: their ultrathin platinum coating and superior electrocatalytic activity toward methanol oxidation', Chem. Mater., 20, 5682–5686, 2008.
16. J. Ge, T. Huynh, Y. Hu, Y. Yin, 'Hierarchical magnetite/silica nanoassemblies as magnetically recoverable catalyst–supports', Nano Lett., 8, 931–934, 2008.
17. Y. Xian, F. Gao, B. Cai, 'Synthesis of platinum nanoparticle chains based on α-chymotrpsin fibrils', Mater. Lett., 111, 39–42, 2013.
18. M. Bhatia, A. Girdhar, B. Chandrakar, A. Tiwari, 'Implicating nanoparticles as potential biodegradation enhancers: a review', J. Nanomed. Nanotechnol., 4, Article no. 2, 2013.
19. I. M. Hamouda, 'Current perspectives of nanoparticles in medical and dental biomaterials', J. Biomed. Res., 26, 143–151, 2012.
20. U. Shanker, V. Jassal, M. Rani, 'Catalytic removal of organic colorants from water using some transition metal oxide nanoparticles synthesized under sunlight', RSC Adv., 6, 94989–94999, 2016.
21. S. S. Raut, O. Bisen, B. R. Sankapal, 'Synthesis of interconnected needle-like Bi_2O_3 using successive ionic layer adsorption and reaction towards supercapacitor application', Ionics, 23, 1831–1837, 2017.
22. S. Murgolo, F. Petronella, R. Ciannarella, R. Comparelli, A. Agostiano, M. L. Curri, G. Mascolo, 'UV and solar-based photocatalytic degradation of organic pollutants by nano-sized TiO_2 grown on carbon nanotubes', Catal. Today, 240, 114–124, 2015.
23. L. Chen, B. Yang, P. Zhou, T. Xu, C. He, Y. Xu, C. Zhao, 'A polyethersulfone composite ultrafiltration membrane with the in-situ generation of CdS nanoparticles for the effective removal of organic pollutants and photocatalytic self-cleaning', J. Membr. Sci., 638, 119715, 2021.

24. P. Duan, R. Su, X. Xu, Q. Li, B. Gao, 'Preparation of Cu_2O-Fe_3O_4@carbon nanocomposites derived from natural polymer hydrogel template for organic pollutants degradation', J. Taiwan Inst. Chem. Eng., 102, 456–464, 2019.
25. X. Qian, H. Xu, X. Zhang, R. Lei, J. Gao, S. Xu, 'Enhanced visible-light-driven photocatalytic activity of Ag_3PO_4/metal–organic framework composite', Polyhedron, 163, 1–6, 2019.
26. G. F. Huang, Z. L. Ma, W. Q. Huang, Y. Tian, C. Jiao, Z. M. Yang, A. Pan, 'Ag_3PO_4 semiconductor photocatalyst: possibilities and challenges', J. Nanomater., 2013, 371356, 2013.
27. P. Xia, Y. J. Song, Y. Z. Liu, M. X. Long, C. Yang, X. Y. Zhang, T. Zhang, 'Advances in the optical and electronic properties and applications of bismuth-based semiconductor materials', J. Mater. Chem. C, 12, 1609–1624, 2024.
28. X. Yang, L. Qu, F. Gao, Y. Hu, H. Yu, Y. Wang, P. Hu, 'High-performance broadband photoelectrochemical photodetectors based on ultrathin Bi2O2S nanosheets', ACS Appl. Mater. Interfaces, 14, 7175–7183, 2022.
29. S. Pang, Y. Dong, D. Xu, Q. Wang, W. Gao, L. Zhang, P. Wang, 'Strong interface interaction and internal electric field promote electron transfer of Bi_2O_2S/$NiFe_2O_4$ heterojunction for photocatalytic antibiotic degradation', J. Mater. Sci. Technol., 158, 145–155, 2023.
30. J. Zhu, X. Zhang, Z. Qin, L. Zhang, Y. Ye, M. Cao, T. Jiao, 'Preparation of PdNPs doped chitosan-based composite hydrogels as highly efficient catalysts for reduction of 4-nitrophenol', Colloids Surf. A, 611, 125889, 2021.
31. H. Jiang, Y. Liu, W. Li, J. Li, 'Co nanoparticles confined in 3D nitrogen-doped porous carbon foams as bifunctional electrocatalysts for long-life rechargeable Zn–air batteries', Small, 14, 1703739, 2018.
32. M. Sharma, G. Sharma, S. Kaushal, R. Badru, 'Eu-Gd@ $BiPO_4$ nano-composite: a potential heterogeneous catalyst in Biginelli reaction', J. Mol. Liq., 384, 122218, 2023.
33. L. Y. Ng, A. W. Mohammad, C. P. Leo, N. Hilal, 'Polymeric membranes incorporated with metal/metal oxide nanoparticles: A comprehensive review', Desalination, 308, 15–33, 2013.
34. G. Jing, L. Wang, H. Yu, W. A. Amer, L. Zhang, 'Recent progress on study of hybrid hydrogels for water treatment', Colloids Surf. A, 416, 86–94, 2013.

35. J. Zhou, B. Hao, L. Wang, J. Ma, W. Cheng, 'Preparation and characterization of nano-TiO_2/chitosan/poly(N-isopropylacrylamide) composite hydrogel and its application for removal of ionic dyes', Sep. Purif. Technol., 176, 193–199, 2017.
36. M. J. Tommalieh, 'Electrical conductivity characterization of Chitosan/Poly(vinyl alcohol) doped by bismuth oxide nanoparticles', Compos. Commun., 25, 100692, 2021.
37. T. Chapple-McGruder, J. P. Leider, A. J. Beck, B. C. Castrucci, E. Harper, K. Sellers, J. Engel, 'Examining state health agency epidemiologists and their training needs', Ann. Epidemiol., 27, 83-88, 2017.
38. G. Lewis, 'Nucleus pulposus replacement and regeneration/repair technologies: present status and future prospects', J. Biomed. Mater. Res. B, 100, 1702–1720, 2012.
39. H. Klinkmann, J. Vienken, 'Membranes for dialysis', Nephrol. Dial. Transplant., 10, 39-45, 1995.
40. J. Sampson, D. De Korte, 'DEHP-plasticised PVC: relevance to blood services', Transfus. Med., 21, 73-83, 2011.
41. M. N. Rittner, T. Abraham, 'Nanostructured materials: An overview and commercial analysis', JOM, 50, 36, 1998.
42. V. Gupta, D. Biswas, S. Roy, 'A comprehensive review of biodegradable polymer-based films and coatings and their food packaging applications', Materials, 15, 5899, 2022.
43. M. A. Kadhim, Z. M. Kadam, 'Adsorption of doxorubicin-hydrochloride onto garlic-loaded chitosan-poly(acrylic acid)/MWCNTs nanocomposite', Appl. Chem. Eng., 8, ACE-5703, 2025.
44. M. Jureczko, J. Kalka, 'Cytostatic pharmaceuticals as water contaminants', Eur. J. Pharmacol., 866, 172816, 2020.
45. R. Dumitru, A. Ianculescu, C. Păcurariu, L. Lupa, A. Pop, B. Vasile, F. Manea, '$BiFeO_3$-synthesis, characterization and its photocatalytic activity towards doxorubicin degradation from water', Ceram. Int., 45, 2789–2802, 2019.
46. H. Du, A. Zhang, Q. Zhang, Y. Sun, H. Zhu, H. Wang, G. Chen, 'Fabrication of recoverable Bi_2O_2S/Bi_5O_7I/ZA hydrogel beads for enhanced photocatalytic Hg0 removal in the presence of H_2O_2', Sep. Purif. Technol., 359, 130597, 2025.

47. X. Zhang, Y. Liu, G. Zhang, Y. Wang, H. Zhang, F. Huang, 'Thermal decomposition of bismuth oxysulfide from photoelectric Bi_2O_2S to superconducting Bi4O4S3', ACS Appl. Mater. Interfaces, 7, 4442–4448, 2015.
48. J. Brugnerotto, J. Lizardi, F. M. Goycoolea, W. Argüelles-Monal, J. Desbrieres, M. Rinaudo, 'An infrared investigation in relation with chitin and chitosan characterization', Polymer, 42, 3569–3580, 2001.
49. Y. Luo, H. Han, J. Li, Q. Wang, W. Zhang, Y. Jia, 'Fe doped Bi_2O_2S nanosheets for improved organic pollutants photo-Fenton degradation and CO2 photoreduction', Sep. Purif. Technol., 306, 122734, 2023.
50. H. Wang, J. J. Zhu, J. M. Zhu, H. Y. Chen, 'Sonochemical method for the preparation of bismuth sulfide nanorods', J. Phys. Chem. B, 106, 3848–3854, 2002.
51. A. K. Sahoo, M. R. Panigrahi, 'Structural analysis, FTIR study and optical characteristics of graphene doped Bi_2O_3 thin film prepared by modified sol–gel technique', Results Chem., 4, 100614, 2022.
52. A. Pawlak, M. Mucha, 'Thermogravimetric and FTIR studies of chitosan blends', Thermochim. Acta, 396, 153–166, 2003.
53. B. Gieroba, A. Sroka-Bartnicka, P. Kazimierczak, G. Kalisz, A. Lewalska-Graczyk, V. Vivcharenko, A. Przekora, 'Spectroscopic studies on the temperature-dependent molecular arrangements in hybrid chitosan/1,3-β-D-glucan polymeric matrices', Int. J. Biol. Macromol., 159, 911–921, 2020.
54. Z. Su, B. Wu, L. Chen, M. T. Mosisa, P. Zhang, Q. Wu, X. Chen, 'Ti-doped $Bi_2(O,S)_3$ bimetal oxysulfide for highly efficient catalytic reduction of organic dyes and heavy metal pollutants in the dark', J. Sci.: Adv. Mater. Devices, 8, 100645, 2023.
55. Y. Alqaheem, A. A. Alomair, 'Microscopy and spectroscopy techniques for characterization of polymeric membranes', Membranes, 10, Article no. 33, 2020.
56. V. Singh, S. Dhukia, L. Khullar, S. Sihag, R. Kaur, K. Harjai, V. Singh, 'Synthesis and Characterization of Biomass Derived Modified Lignin Based PVA Hydrogel as Drug Delivery System for Ciprofloxacin', ChemistrySelect, 10, e202404597, 2025.
57. S. K. Singh, A. Kumar, B. Gahtori, Shruti, G. Sharma, S. Patnaik, V. P. Awana, 'Bulk superconductivity in bismuth oxysulfide $Bi_4O_4S_3$', J. Am. Chem. Soc., 134, 16504–16507, 2012.

58. I. Corazzari, R. Nisticò, F. Turci, M. G. Faga, F. Franzoso, S. Tabasso, G. Magnacca, 'Advanced physico-chemical characterization of chitosan by means of TGA coupled on-line with FTIR and GCMS: Thermal degradation and water adsorption capacity', Polym. Degrad. Stab., 112, 1–9, 2015.

59. N. Singh, D. Sharma, M. Thakur, A. Dan, 'Zinc oxide-loaded chitosan-graphene oxide hydrogel nanocomposite as a potential catalyst for photocatalytic dye degradation', Int. J. Biol. Macromol., 308, 142424, 2025.

60. L. S. Guinesi, É. T. G. Cavalheiro, 'The use of DSC curves to determine the acetylation degree of chitin/chitosan samples', Thermochim. Acta, 444, 128–133, 2006.

61. P. R. Jubu, O. S. Obaseki, D. I. Ajayi, E. Danladi, K. M. Chahrour, A. Muhammad, F. K. Yam, 'Considerations about the determination of optical bandgap from diffuse reflectance spectroscopy using the Tauc plot', J. Opt., 53, 5054–5064, 2024.

62. D. Sharma, S. Kaur, S. Bansal, P. Kaur, S. Singhal, 'Building a potentially active NiFe2O4 embedded lignin framework for adsorption coupled photocatalytic degradation and fluorescence detection of doxorubicin and safranin-O', React. Funct. Polym., 106589, 2025.

63. Abhivyakti., P. Kaur, D. Aggarwal, S. Singhal, 'Defect-engineered C, N-ZnO/Co_3O_4/$CoFe_2O_4$/Fe_3O_4 for ultra-fast tetracycline degradation and environmental impact assessment using an in silico mathematical model', Adv. Compos. Hybrid Mater., 8, Article no. 156, 2025.

64. S. Balasurya, M. K. Okla, H. AbdElgawad, A. A. Al-Ghamdi, M. A. Abdel-Maksoud, S. S. Al-Amri, S. S. Khan, 'Self-propelled nanojets an interfacial Schottky junctions modulated oxygen vacancies enriched for enhanced photo-Fenton degradation of organic contaminant: Improving H_2O_2 generation, Fe^{3+}/Fe^{2+} cycle and enhancing plant metabolism', Chemosphere, 314, 137516, 2023.